Supporting Information for "Deglacial ice sheet instabilities induced by proglacial lakes"

Aurélien, Quiquet[1], Christophe, Dumas[1], Didier, Paillard[1],Gilles, Ramstein[1],

Catherine, Ritz[2], Didier M., Roche[1,3]

[1]Laboratoire des Sciences du Climat et de l'Environnement, LSCE/IPSL, CEA-CNRS-UVSQ, Université Paris-Saclay, F-91191 Gif-sur-Yvette, France

[2]Université Grenoble Alpes, CNRS, IRD, Grenoble INP, IGE, 38000 Grenoble, France

[3]Vrije Universiteit Amsterdam, Faculty of Science, Cluster Earth and Climate, de Boelelaan 1085, 1081HV Amsterdam, The Netherlands

Contents of this file

Corresponding author: A. Quiquet, Laboratoire des Sciences du Climat et de l'Environnement, LSCE/IPSL, CEA-CNRS-UVSQ, Université Paris-Saclay, F-91191 Gif-sur-Yvette, France (aurelien.quiquet@lsce.ipsl.fr)

Introduction

This supplement contains additional material on our model experiments. Text S1 provides further information on the methods used. Text S2 discusses simulated ice sheet evolution agreement with geologically-constrained reconstructions and timing of the proglacial lake ice sheet instability. Text S3 quantifies the respective role of surface and basal mass balance with respect to ice discharge. Text S4 and S5 provides more information on the lake water depth and on the sensitivity of the ice sheet instability to sub-shelf melting and calving rates. Finally Text S6 is a discussion on the role of the millenial atmospheric variability in the stand-alone experiments. Fig. S1 to S11 are additional figures to expend the analyses of the main text and the discussions raised in the this supporting information.

Text S1. Extended descriptions of methods

Ice sheet model

The ice model used in this study is GRISLI v2 (Quiquet, Dumas, et al., 2018). This model is a recently updated version of the GRISLI model which has been extensively used to study ice and climate interactions for a variety of scientific questions across timescales and in particular for Pleistocene Northern Hemisphere ice sheets. GRISLI is a thermo-mechanically coupled model that uses a combination of the shallow shelf and shallow ice approximations. The sub-grid position of the grounding line is computed with a linear interpolation of the flotation criteria (the difference between the ice load and the buoyancy force). The analytical ice flux at the grounding line (Tsai et al., 2015) is

linearly interpolated to the neighbouring velocity grid points. Calving at the ice shelf front is based on a simple cut-off thickness threshold of 250 metres below which ice is calved. Glacial isostasy is accounted for with an elastic lithosphere - relaxed asthenosphere model. Any grid point falling below the contemporaneous eustatic sea level is assumed to be flooded with a water surface elevation at the eustatic sea level value. For the work presented here, we use a 40-km Cartesian grid covering the Northern Hemisphere. For model calibration, we performed a model parameter tuning in which we sampled out four critical parameters (shallow ice enhancement factor, basal drag coefficient, till conductivity for the sub-glacial hydrology model and sub-shelf basal melting rates) with a latin hypercube (Quiquet, Dumas, et al., 2018) of 300 ensemble members. We assumed that the parameters yielded for Antarctica are valid for the Northern Hemisphere ice sheets and we selected the ensemble member that has the lowest root mean square error with respect to the present-day observed Antarctic topography. Unlike Quiquet, Dumas, et al. (2018) we use a present-day Northern Hemisphere sediment thickness distribution to locally enhance basal sliding. Where the sediment thickness is greater than 200 metres, we apply a dimensionless factor of 0.05 to the basal drag coefficient. This is consistent with our knowledge of basal sliding (facilitated over water-saturated till) and ensures a reasonable simulated ice volume at the last glacial maximum (LGM), with an in ice volume difference lower than 10% with respect to ICE-6G_C. Bedrock topography is taken from ETOPO1 and the geothermal heat flux is spatially variable. Both are regridded to the 40-km grid using bilinear interpolation.

Coupled experiments

We used the coupled iLOVECLIM-GRISLI model (Roche, Dumas, et al., 2014). The core of the iLOVECLIM climate model consists of a spectral T21 atmospheric model (ECBilt), a vegetation model (VECODE) and a sea ice and 3D free surface ocean (CLIO). Since Roche, Dumas, et al. (2014), the coupling with the ice sheet model has been improved in several important ways. While the surface mass balance was computed with a positive degree day model from bilinearly interpolated atmospheric fields, we now make use of a downscaling scheme (Quiquet, Roche, et al., 2018) to compute a surface mass balance at each atmospheric model time step, using an insolation-temperature-melt model (ITM) (van den Berg et al., 2008). We use absolute fields, namely surface mass balance and near-surface air temperature, without bias correction to force the ice sheet model. In addition, for floating ice shelves, instead of using an ad-hoc prescribed sub-shelf basal melting rate, we compute the melt from temperature and salinity provided by the ocean model (Beckmann & Goosse, 2003). Since the ice sheet model does not distinguish the lakes from the ocean, floating ice grid points that fall outside the oceanic domain, use the nearest oceanic condition to compute sub-shelf melting. This is an important simplification as the lake thermodynamics in lakes is largely different from the one in the ocean (Benn et al., 2007). For this reason, we use a wide range of sub-shelf melting rate and calving threshold and show only a very limited change on the results (supporting information, Fig. S9). Although the model is computationally cheaper than complex general circulation model, our setup requires a substantial amount of time to compute the whole deglaciation, as we require 24 hours to compute approximatively 500 years using 8 processors on our local cluster. For this reason, we use an acceleration factor of 10 for

the external forcings (greenhouse gases and orbital configuration). The ice sheet model is run 10 years for 1 year of climate and the coupling frequency is 1. With this setup, the mass conservation of water between the ice sheet model and the rest of the climate model cannot be preserved and as such the hydrological budget is computed without considering the effect of the ice sheet. This prevents the eventual feedbacks between ice sheet volume reduction and Atlantic meridional overturning circulation (AMOC) and the related non-linearities of the climate evolution through the deglaciation. For example, in our experiment we have a deep and active AMOC at the last glacial maximum (∼17 Sv, with 1 Sv = 10^6 m^3 s^{-1}) that gradually slows down by 30% towards its Holocene values (∼12 Sv). The ITM model has a largely unconstrained free parameter (constant c in van den Berg et al. (2008)). With a homogeneous value of this constant, the NAIS retreats systematically before the Eurasian ice sheet. This temporal mismatch is probably the result of atmospheric biases in the iLOVECLIM model that presents a substantial excessive warmth over North America and a moderate cold bias in the Kara-Barents region for the present-day simulated climate (Heinemann et al., 2014). For this reason we use a geographically variable value for the constant c (varying from about -80 W m^{-2} around present-day Hudson Bay to 0 W m^{-2} in the Kara Sea), based on the present-day temperature bias with respect to ERA-interim (Dee et al., 2011). In order to avoid initial model drift, the following methodology was used:

i- We run first iLOVECLIM for 5000 years under LGM boundary conditions (greenhouse gases and orbital forcing) and with prescribed ice sheets of GLAC-1D. We use the last hundred years of this simulation to generate climatological surface mass balance and sur-

face temperature forcings needed by the ice sheet model.

ii- Using these forcing fields, the ice sheet model is run offline for 100 ka to reach equilibrium.

iii- Finally, we use the spun-up climate (after the 5000 years) of step i as an initial conditions for our deglacial simulations, replacing the GLAC-1D ice sheets by the spun-up ice sheets of ii.

In the climate model, the bathymetry is left unchanged in our experiments. We used a last glacial maximum bathymetry from a previous study (Roche, Paillard, et al., 2014).

Ice sheet stand-alone experiments

For stand-alone experiments we use a simple index method (Charbit et al., 2007). We computed LGM climate anomalies with respect to the pre-industrial from general circulation model outputs of the PMIP3 database (Abe-Ouchi et al., 2015). For the LGM, the monthly near-surface air temperature differences are added on top of the ERA-interim (Dee et al., 2011) 1989-2008 monthly climatologies. Similarly, the monthly precipitation ratio is multiplied by the monthly total precipitation of the 1989-2008 climatology. As in Charbit et al. (2007), the LGM climate anomalies are weighted in time so that the climate forcing for the present-day is entirely the result of the ERA-interim forcing field:

$$\Delta X\left(t\right) = \left(1 - \alpha\left(t\right)\right) \Delta X_{LGM} \tag{1}$$

with X being monthly temperature or total precipitation and α the time dependent glacial index (0 at the LGM and 1 at 0 kaBP). However, while in Charbit et al. (2007) the glacial index α was purely linear in time, for this work an additional term that accounts for the

fast atmospheric variability recorded as in ice cores is used:

$$\alpha(t) = r \times \xi(t) + (1 - r) \times \zeta(t) \quad (2)$$

with ξ which follows the North GRIP δ^{18}O and which is scaled so it is 0 at the LGM and 1 at 0 kaBP. The slow orbital variability, ζ , is simply the time from the LGM, with a value of 0 for the LGM at 21 kaBP and 1 at 0 kaBP. The weighting factor, r, is an unknown parameter which has important consequences on the imposed climatic scenarios. In addition, it is a simplification to assume atmospheric synchronicity and similar amplitude of changes between the Greenland and North America ice sheets. For this reason, for a given GCM climate forcing, we run various possibilities for r: 0.15, 0.25, 0.35, 0.45 and 0.55 (a high value meaning that more importance is given to rapid, millenial, variability with respect to orbital variability, Fig. S10). The reference value for the figures shown in the manuscript is 0.25, which corresponds to a limited importance of the fast variability, with a transition from the LGM to the pre-industrial almost linear (Fig. S10). The rapid variability tends to accelerate the ice loss and produces larger MWP-1A event. However, in this case, even though the event happens earlier in the deglaciation (Fig. S10), the PLISI continues to play a crucial role when flotation is reached at the southern margin of the ice sheet. We also use a constant and homogeneous vertical lapse rate of 6 ° C km^{-1} to account for temperature changes due to topography changes. Precipitation is corrected using the same temperature-precipitation relationship as in Charbit et al. (2007). From the various GCM outputs in the PMIP3 database, we selected the five that produce reasonable ice sheet geometries at the LGM: FGOALS-g2, IPSL-CM5A-LR, MPI-ESM-P, MIROC-ESM and GISS-E2-R. Other climate forcings in the PMIP3 database produced too small ice

sheets (e.g. CNRM-CM5 or MRI-CGCM3). The surface mass balance is computed with a positive degree day model. For the oceanic forcing we use a two value sub-shelf basal melting rate (continental shelf, 0.2 m yr^{-1}, and deep ocean, 10 m yr^{-1} under present-day conditions) perturbed by an index for the strength of the AMOC calculated from a North Atlantic benthic foraminifera record (Quiquet, Dumas, et al., 2018). Similarly to the coupled simulations, the initial ice sheet conditions for the stand-alone experiments are the spun-up ice sheets from the equilbrium simulations under perpetual LGM climatic forcing field computed from iLOVECLIM. The simulations are transient and span the last 26 ka.

Text S2. Agreement with geologically-constrained reconstructions and timing of the event

Our knowledge of individual ice volume for the different ice sheets across the last deglaciation is mostly known from comprehensive inverse methods applied to indicators for modern surface subsidence measurements and radiocarbon dated archives for relative sea level evolution. Two major reconstructions are publicly available in the literature. The ICE-6G_C VM5a model (ICE-6G_C in the manuscript)(Peltier et al., 2015) makes use of the most complete dataset used to constrain the local ice thickness history while the global ice mass is constrained by eustatic sea level curves. The GLAC-1D model (Tarasov et al., 2012; Ivanovic et al., 2016) is a compilation of various works and it differs from ICE-6G_C by the inclusion of a comprehensive ice sheet model and fewer degrees of freedom in the inversion procedure. If the two reconstructions agree generally very well with respect to the ice extent history, the ice volume is nonetheless largely different. For the NAIS,

there is more than 5 million cubic kilometres (more than 10 metres of sea level equivalent) of ice volume difference between the two reconstructions. The GLAC-1D model shows a lower ice volume and a thinner ice sheet for the LGM. The transient evolution is also very different. Thus, if both reconstructions suggest a NAIS contribution to the MWP-1A of about 3 m of global sea level equivalent (mSLE) per century, they disagree for the latest stage of the deglaciation. The ICE-6G_C reconstruction shows a gradual ice volume reduction after 14 kaBP while GLAC-1D shows a pause in ice loss during the Younger Dryas and two pulses (between 12 and 11 kaBP and later between 9 and 8 kaBP). Towards the end of the Younger Dryas, GLAC-1D shows a NAIS collapse at a rate of 1.5 mSLE. Although this feature of the late deglacial NAIS is absent from ICE-6G_C, using the same glacial isostatic data but including an updated ice sheet model, a recent study (Stuhne & Peltier, 2017) has also suggested that a collapse of the late deglacial NAIS could explain the MWP-1B. These differences between two geophysically-constrained reconstructions are due to a poor understanding of the Earth rheology and its spatial and temporal evolution but also to some different interpretations of archives for relative sea level changes. Our approach is drastically different since it does not involve any inversion of palaeo-data and as such there is no a priori on the relative importance of the different processes.

The simulated ice sheet extent topography for the last glacial maximum (21 kaBP) in the coupled experiment is shown in Fig. S1. The extent is in generally good agreement with the geophysically-constrained reconstructions of ICE-6G_C and GLAC-1D, except in western Eurasia where it is underestimated. The spun-up ice sheet used as initial conditions for our transient experiments was obtained after a long (100 ka) ice sheet simulation

under perpetual LGM climate forcing provided by iLOVECLIM. It shows a good agreement in term of volume with both geophysically-constrained reconstructions. However, the coupling that starts at 26 kaBP induces a slight volume increase from 26 kaBP to 21 kaBP, in contradiction with ICE-6G_C and GLAC-1D that show a volume reduction within this time frame. Because the extent is almost unchanged from 26 to 21 kaBP in our coupled simulation, this means that our simulated ice sheet is getting thicker, increasing the mismatch with the two reconstructions. Later in the deglaciation the iLOVECLIM-GRISLI setup produces overestimated melt rates which lead to an underestimation of the ice extent of the NAIS, especially at its southern margin (Fig. S2). This is in part related to the warm bias in the model over North America(Heinemann et al., 2014) and also because there is no feedback of ice sheet volume reduction on North Atlantic overturning circulation. This too early deglaciation introduces a temporal mismatch between the geophysically-constrained reconstructions and the model results, the latter showing a lead of more than 2000 years in some places. As such the coupled simulations offer a weak constraint on the timing of the PLISI, except that its occurrence requires a reduced ice sheet in order to reach the flotation criterion. The stand-alone experiments generally show a much better temporal agreement with the geophysically-constrained reconstructions since in this case the climatic temporal evolution is partly driven by the Greenland temperature variation reconstruction. However, even amongst the stand-alone experiments, the different GCMs produce drastically different NAIS ice sheet evolutions.

Since the PLISI is initially triggered by the floatation criterion, the sensitivity of the simulated NAIS geometry evolution to the climate forcing explains the diversity in terms

of timing of the event, which can be as early as 13.8 kaBP to as late as 9.6 kaBP (Fig. S4). Given these uncertainties in term of forcings and ice sheet geometry evolution, the model experiments only offer a weak constraints on the timing of the PLISI. Nonetheless, to happen it requires a reduce ice sheet size (to reach floatation). The experiments that have the best agreement with the geophysically-constrained reconstructions tend to show a PLISI happening between 9 and 11 kaBP.

Text S3. Respective role of surface and basal mass balance with respect to ice discharge

The study of the different terms of the mass conservation equation can help us to quantify the respective role of mass balance induced by climate change and mass balance that results from ice discharge. The mass conservation equation is the following:

$$\frac{\partial H}{\partial t} = B - \nabla\left(\boldsymbol{u}H\right) \tag{3}$$

where H is the ice thickness, B is the sum of the surface and basal mass balance and $\boldsymbol{u}$ is the horizontal velocity (i.e. $\nabla\left(\boldsymbol{u}H\right)$ is the ice divergence).

Fig. S5 shows the breakdown of the different terms of Eq. 3 for two snapshots that encompass the maximum rate of volume change in the coupled simulation. Before the event, the melt at the southern margin (Fig. S5a) is partly compensated by the ice flux convergence (Fig. S5b) and the pattern of ice thickness change (Fig. S5c) resembles the one of surface and basal mass balance. Once the PLISI is triggered, the large ice thinning in the vicinity of the proglacial lake grounding line (Fig. S5f) is almost entirely explained

by the increased ice flux divergence (Fig. S5e). This shows that if the event is initially triggered by a decrease in surface mass balance, it is nonetheless almost entirely mechanically driven and, as such, independent from any later climate change.

Text S4. Proglacial lake water depth

Since the proglacial lake ice sheet instability is a grounding line instability its trigger is strongly dependent on the water depth at the grounded margin. The accurate modelling of proglacial lakes requires a very high resolution of the palaeo-topography to compute a precise routing of melt-water. It also requires a high confidence in the simulated palaeo-topography since departures from observational ice sheet extent can drastically change the route for melt water. Given the diversity in simulated palaeo-topographies (e.g. Fig. S4) an interactive scheme for proglacial lakes will produce a wide range of lake surface elevations. However, a recent attempt to interactively compute proglacial lake drainage has been made in a large scale ice sheet model with promising results(Berends & Wal, 2016).

Our ice sheet model does not yet simulate explicitly proglacial lakes. In the standard version of the model, any depression below the contemporaneous eustatic sea level is considered flooded with a surface elevation being at the eustatic sea level. This is in fact a conservative estimate since the hydrological budget of these mid- to high-latitude lakes was probably positive and, as such, their surface elevation will be equal to the topographic barrier along the route towards the ocean. With this conservative estimate, we systematically produce a grounding line instability (Fig. S4). Any more realistic changes in lake level in the course of the deglaciation would result in a larger ice sheet volume

reduction due to the PLISI. To infer a more realistic value for the lake surface elevation consistent with our modelling results, we built for this paper a depression-filling algorithm. This algorithm computes a connectivity graph that minimises the topographic barrier that separates two given points. We run the algorithm for one snapshot within the deglaciation and selecting one point in the proglacial lake and one in the Atlantic ocean. For the palaeo-topography, we use a North American subset of the ETOPO1 digital elevation model in which we superpose the simulated anomaly with respect to the present-day topography. The outputs of our algorithm is shown in Fig. S6. We found a lake surface elevation at about 160 m above present-day sea level, which is about 235 m above the contemporaneous eustatic sea level, a value close to what has been found in other studies(Clarke et al., 2004). This difference with respect to the coeval sea level is substantial and would have an impact of the magnitude of the PLISI. With additional sensitivity experiments in which we assume a constant lake surface elevation at +50 m above present-day sea level, we considerably amplify the importance of the PLISI (Fig. S7 and Fig. S8) and we expect an even more amplified effect with +160 m above present-day sea level as found in our depression-filling algorithm.

Text S5. Calving events and sub-shelf melt rates in proglacial lakes

The proglacial lake ice sheet instability mechanism leads to a massive solid ice discharge into the lake. While in Antarctica ice shelf thinning and associated calving are mostly controlled by the oceanic thermal forcing, proglacial lakes may remain relatively cold throughout the year with a limited available heat to melt the ice shelves(Trüssel et al.,

2013). In addition, present-day freshwater calving glaciers display lower calving rates than their tidewater analogues(Benn et al., 2007). Using different simulations for which we drastically reduce the calving rate, we show that the volume of the ice shelves is not much larger than in the standard experiment and that the grounded ice volume is virtually not changed (Fig. S9). This is because surface mass balance at the southern margin of the ice sheet is strongly negative (surface ablation of several metres per year) and does not allow maintaining an ice shelf (surface ablation greater than ice flux convergence). As a result, calving of the ice at the front plays only a minor role and our experiments are weakly sensitive to its representation in the model. Similarly, we have also performed experiments in which we reduce the sub-shelf basal melting rates and we arrive at the same conclusions (Fig. S9). The predominant role of surface melt in our experiments with respect to sub-glacial processes is a major difference with the dynamics of present-day Antarctic ice shelves.

We need to acknowledge, however, that for different time intervals and/or ice sheets presenting a colder climate with more limited ice ablation at the surface, the effect of sub-shelf melting and calving might be more important. In which case, a specific lake model could be envisioned.

Text S6. Role of the millenial atmospheric variability in the stand-alone experiments

Contrary to the coupled experiment, most of the stand-alone experiments show an important acceleration of ice volume loss at the time of the Bølling warming, which coin-

cides with the MWP-1A. This result is a direct consequence of the methodology chosen for the stand-alone experiments in which the abrupt warming recorded in Greenland is used to compute the temperature change over the NAIS. However, the synchronicity and amplitude of temperature change over the Greenland ice sheet and the NAIS is questionable. The weighting factor r (see methods) is used to modify the importance given to the millenial atmospheric variability recorded in Greenland: for an extreme value of 1 the temperature changes over the NAIS are entirely driven by the Greenland record whereas for a value of 0 there is a linear transition from the last glacial maximum to the pre-industrial forcing. Fig. S10 shows the rate of ice loss for different values of this atmospheric variability weighing factor r for a given GCM forcing (the associated glacial index is shown in Fig. S11). For greater values, there is an important ice sheet collapse during the Bølling warming while for smaller values the deglaciation is smoother. In contrast, the second deglacial pulse towards the end of the Younger Dryas is systematically present, independently from the fast atmospheric variability chosen. The magnitude of this second pulse is about 2 metres per century for all the different combinations and is closely tight to the PLISI. With these sensitivity experiments, we thus show that the evolution of the rate of ice loss for low value of the fast variability factor resembles the one of the coupled experiment. This is somewhat expected since the coupled model failed to capture the abrupt climatic transition during the deglaciation. Nonetheless, these experiments confirm the importance of the PLISI which systematically occurs regardless of the climatic scenario to drive the ice sheet model.

References

Abe-Ouchi, A., Saito, F., Kageyama, M., Braconnot, P., Harrison, S. P., Lambeck, K., ... Takahashi, K. (2015, November). Ice-sheet configuration in the CMIP5/PMIP3 Last Glacial Maximum experiments. *Geoscientific Model Development*, *8*(11), 3621–3637. doi: 10.5194/gmd-8-3621-2015

Beckmann, A., & Goosse, H. (2003). A parameterization of ice shelfocean interaction for climate models. *Ocean Modelling*, *5*(2), 157–170. doi: 10.1016/S1463-5003(02)00019-7

Benn, D. I., Warren, C. R., & Mottram, R. H. (2007, June). Calving processes and the dynamics of calving glaciers. *Earth-Science Reviews*, *82*(3), 143–179. doi: 10.1016/j.earscirev.2007.02.002

Berends, C. J., & Wal, R. S. W. v. d. (2016, December). A computationally efficient depression-filling algorithm for digital elevation models, applied to proglacial lake drainage. *Geoscientific Model Development*, *9*(12), 4451–4460. doi: 10.5194/gmd-9-4451-2016

Charbit, S., Ritz, C., Philippon, G., Peyaud, V., & Kageyama, M. (2007, January). Numerical reconstructions of the Northern Hemisphere ice sheets through the last glacial-interglacial cycle. *Climate of the Past*, *3*, 15–37.

Clarke, G. K. C., Leverington, D. W., Teller, J. T., & Dyke, A. S. (2004, February). Paleohydraulics of the last outburst flood from glacial Lake Agassiz and the 8200BP cold event. *Quaternary Science Reviews*, *23*(3), 389–407. doi: 10.1016/j.quascirev.2003.06.004

Dee, D. P., Uppala, S. M., Simmons, A. J., Berrisford, P., Poli, P., Kobayashi, S., ... Vitart, F. (2011, April). The ERA-Interim reanalysis: configuration and performance of the data assimilation system. *Quarterly Journal of the Royal Meteorological Society*, *137*(656), 553–597. doi: 10.1002/qj.828

Heinemann, M., Timmermann, A., Elison Timm, O., Saito, F., & Abe-Ouchi, A. (2014). Deglacial ice sheet meltdown: orbital pacemaking and CO2 effects. *Clim. Past*, *10*(4), 1567–1579. doi: 10.5194/cp-10-1567-2014

Ivanovic, R. F., Gregoire, L. J., Kageyama, M., Roche, D. M., Valdes, P. J., Burke, A., ... Tarasov, L. (2016). Transient climate simulations of the deglaciation 21–9 thousand years before present (version 1) PMIP4 Core experiment design and boundary conditions. *Geoscientific Model Development*, *9*(7), 2563–2587. doi: 10.5194/gmd-9-2563-2016

Peltier, W. R., Argus, D. F., & Drummond, R. (2015). Space geodesy constrains ice age terminal deglaciation: The global ICE-6G_c (VM5a) model. *Journal of Geophysical Research: Solid Earth*, *120*(1), 450–487. doi: 10.1002/2014JB011176

Quiquet, A., Dumas, C., Ritz, C., Peyaud, V., & Roche, D. M. (2018, dec). The GRISLI ice sheet model (version 2.0): calibration and validation for multi-millennial changes of the Antarctic ice sheet. *Geoscientific Model Development*, *11*(12), 5003–5025. doi: 10.5194/gmd-11-5003-2018

Quiquet, A., Roche, D. M., Dumas, C., & Paillard, D. (2018, feb). Online dynamical downscaling of temperature and precipitation within the *i*LOVECLIM model (version 1.1). *Geoscientific Model Development*, *11*(1), 453–466. doi: 10.5194/

gmd-11-453-2018

Roche, D. M., Dumas, C., Bügelmayer, M., Charbit, S., & Ritz, C. (2014, July). Adding a dynamical cryosphere to iLOVECLIM (version 1.0): coupling with the GRISLI ice-sheet model. *Geosci. Model Dev.*, *7*(4), 1377–1394. doi: 10.5194/gmd-7-1377-2014

Roche, D. M., Paillard, D., Caley, T., & Waelbroeck, C. (2014, December). LGM hosing approach to Heinrich Event 1: results and perspectives from datamodel integration using water isotopes. *Quaternary Science Reviews*, *106*, 247–261. doi: 10.1016/j.quascirev.2014.07.020

Stuhne, G. R., & Peltier, W. R. (2017). Assimilating the ICE-6G_c Reconstruction of the Latest Quaternary Ice Age Cycle Into Numerical Simulations of the Laurentide and Fennoscandian Ice Sheets. *Journal of Geophysical Research: Earth Surface*, *122*(12), 2324–2347. doi: 10.1002/2017JF004359

Tarasov, L., Dyke, A. S., Neal, R. M., & Peltier, W. R. (2012, January). A data-calibrated distribution of deglacial chronologies for the North American ice complex from glaciological modeling. *Earth and Planetary Science Letters*, *315-316*, 30–40. doi: 10.1016/j.epsl.2011.09.010

Trüssel, B. L., Motyka, R. J., Truffer, M., & Larsen, C. F. (2013). Rapid thinning of lake-calving Yakutat Glacier and the collapse of the Yakutat Icefield, southeast Alaska, USA. *Journal of Glaciology*, *59*(213), 149–161. doi: 10.3189/2013J0G12J081

Tsai, V. C., Stewart, A. L., & Thompson, A. F. (2015). Marine ice-sheet profiles and stability under Coulomb basal conditions. *Journal of Glaciology*, *61*(226), 205–215. doi: 10.3189/2015JoG14J221

van den Berg, J., van de Wal, R., & Oerlemans, H. (2008, April). A mass balance model for the Eurasian Ice Sheet for the last 120,000years. *Global and Planetary Change*, *61*(3), 194–208. doi: 10.1016/j.gloplacha.2007.08.015

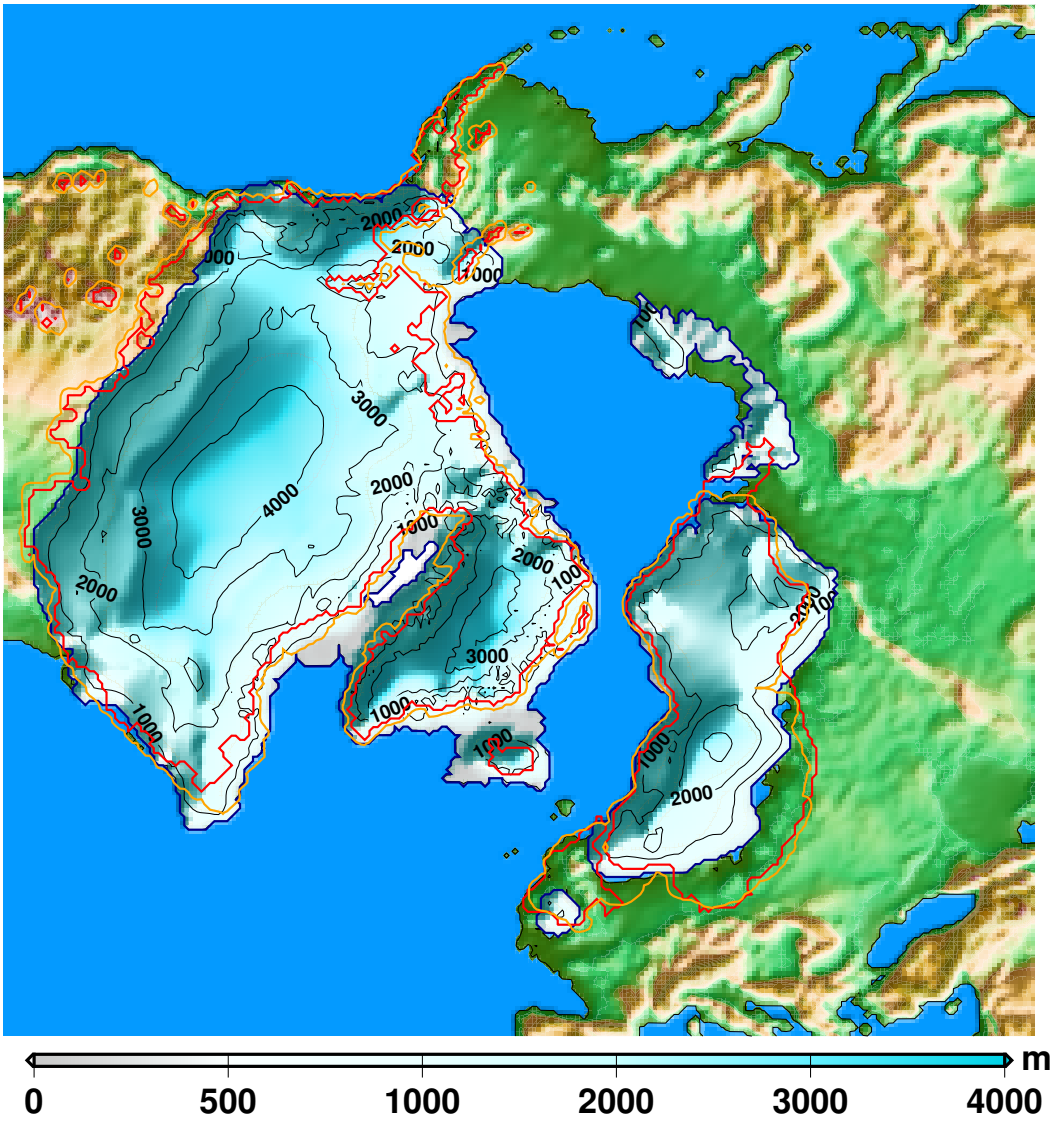

Figure S1. Simulated Northern Hemisphere ice sheets with iLOVECLIM-GRISLI at the last glacial maximum (21 kaBP). Isocontours for ice thickness are represented every 1000 metres and the grounding line is the dark blue line. The extent of ICE-6G_C and GLAC-1D are depicted in red and orange, respectively.

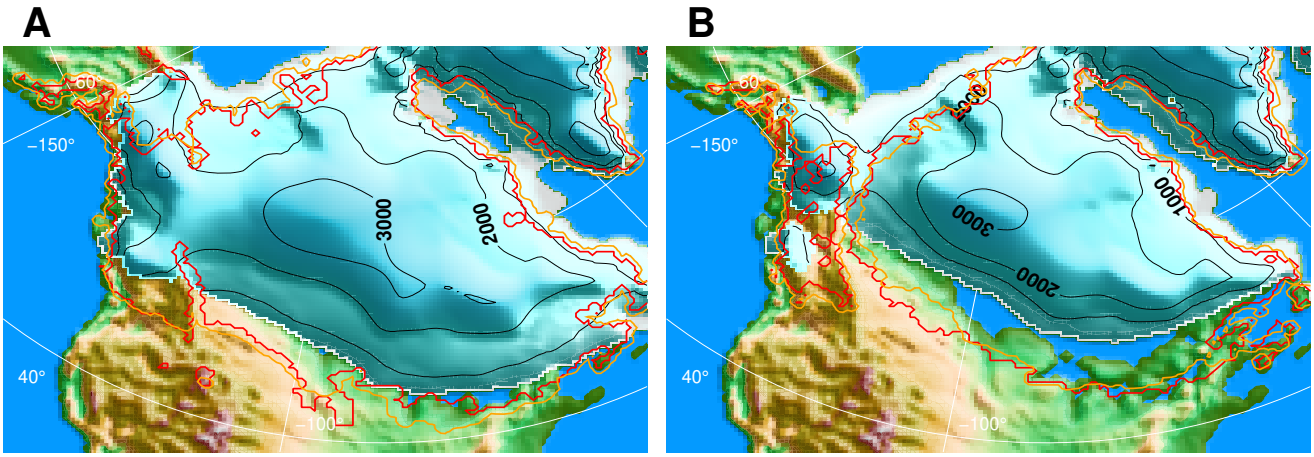

Figure S2. Simulated NAIS at the early stages of the deglaciation. Simulated NAIS with iLOVECLIM-GRISLI at 16 kaBP (A) and at 14 kaBP (B). Isocontours for ice thickness are represented every 1000 metres. The extent of ICE-6G_C and GLAC-1D are depicted in red and orange, respectively.

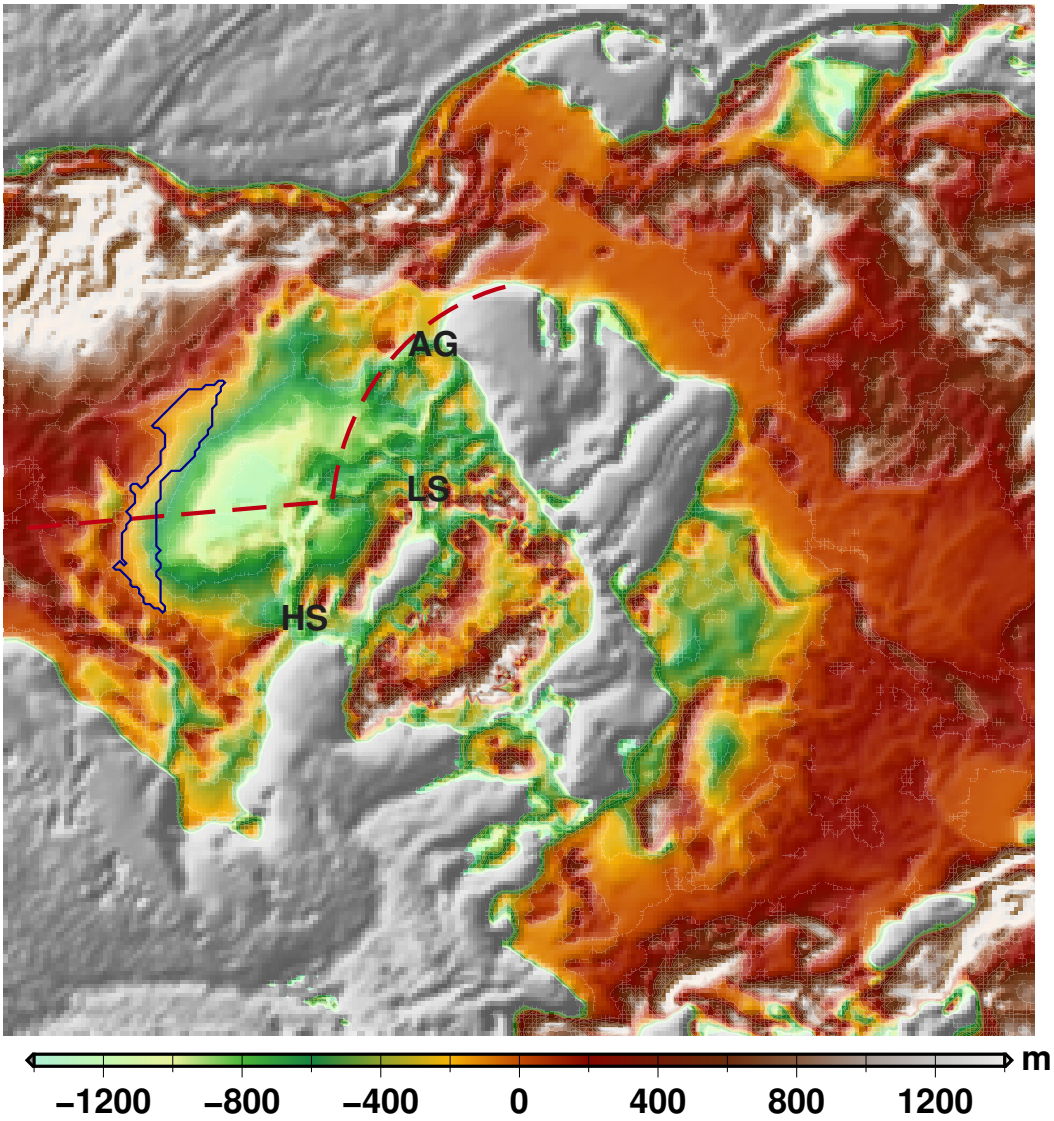

Figure S3. Simulated bedrock topography with iLOVECLIM-GRISLI at 13.8 kaBP. Elevation given in metres above present-day sea level. The simulated extent of proglacial lake Agassiz-Ojibway is contoured dark blue line. The dashed red line represents the ice sheet cross-section presented in the manuscript. The ice streams discussed in the text are: Amundsen Gulf (AG), Lancaster Sound (LS) and Hudson Strait (HS).

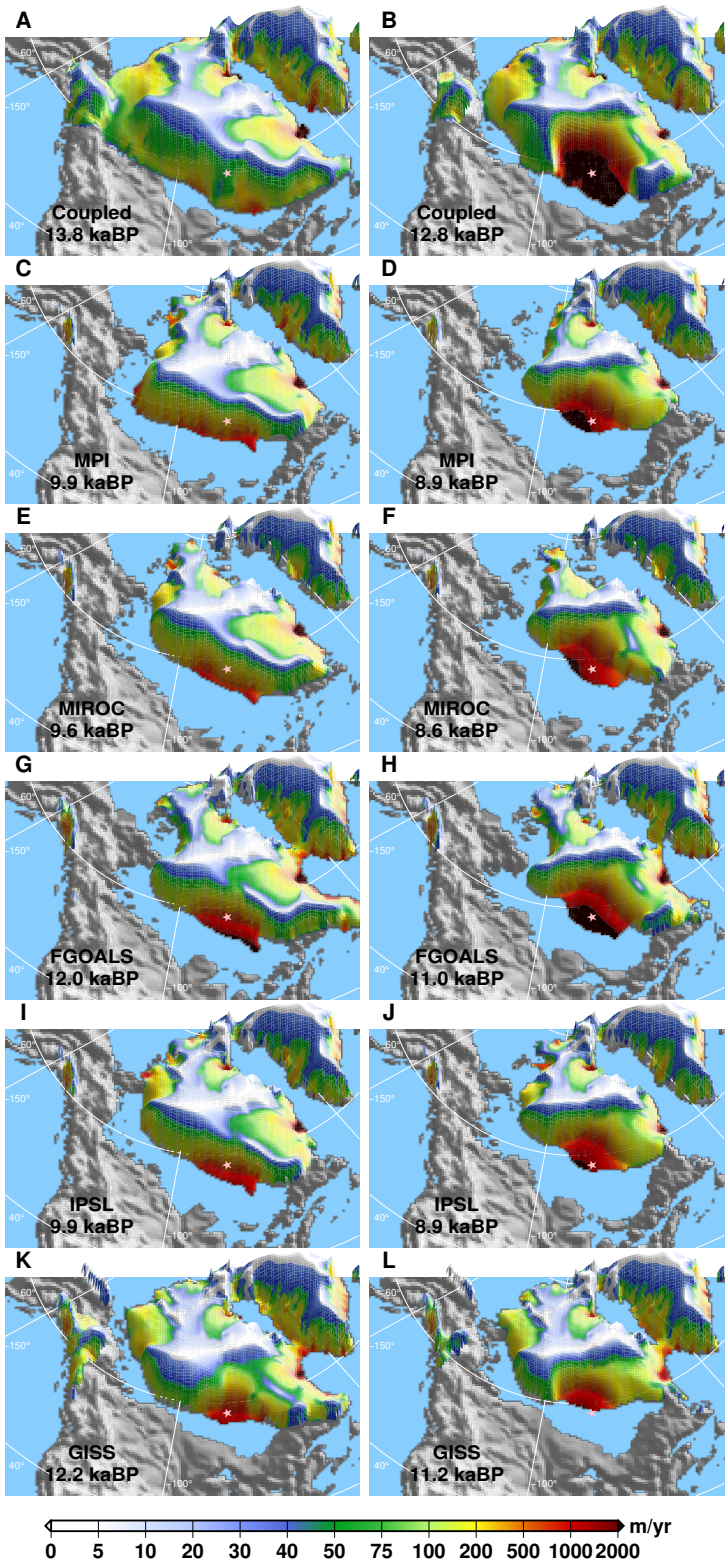

Figure S4. Ice sheet geometries at the time of the instability. Vertically integrated velocity before (left) and after (right) the maximum in rate of NAIS ice loss. Each row corresponds to a specific climate scenario: the coupled experiment (A,B) and the five stand-alone experiments using MPI-ESM-P (C,D), MIROC-ESM (E,F), FGOALS-g2 (G,H), IPSL-CM5A-LR (I,J) and GISS-E2-R (K,L). The stand-alone experiments shown here use a weighing factor for the fast variability of 0.25. For a given climate scenario, the two snapshots presented here are separated by one thousand year with the left-hand side at 13.8 kaBP (A), 9.9 kaBP (C), 9.6 kaBP (E), 12.0 kaBP (G), 9.9 kaBP (I) and 12.2 kaBP (K). For this 3-D perspective plot, the velocity is draped on top of the ice sheet topography. The pink star is the selected grid point for the time evolution of the ice flux shown in Fig. S8.

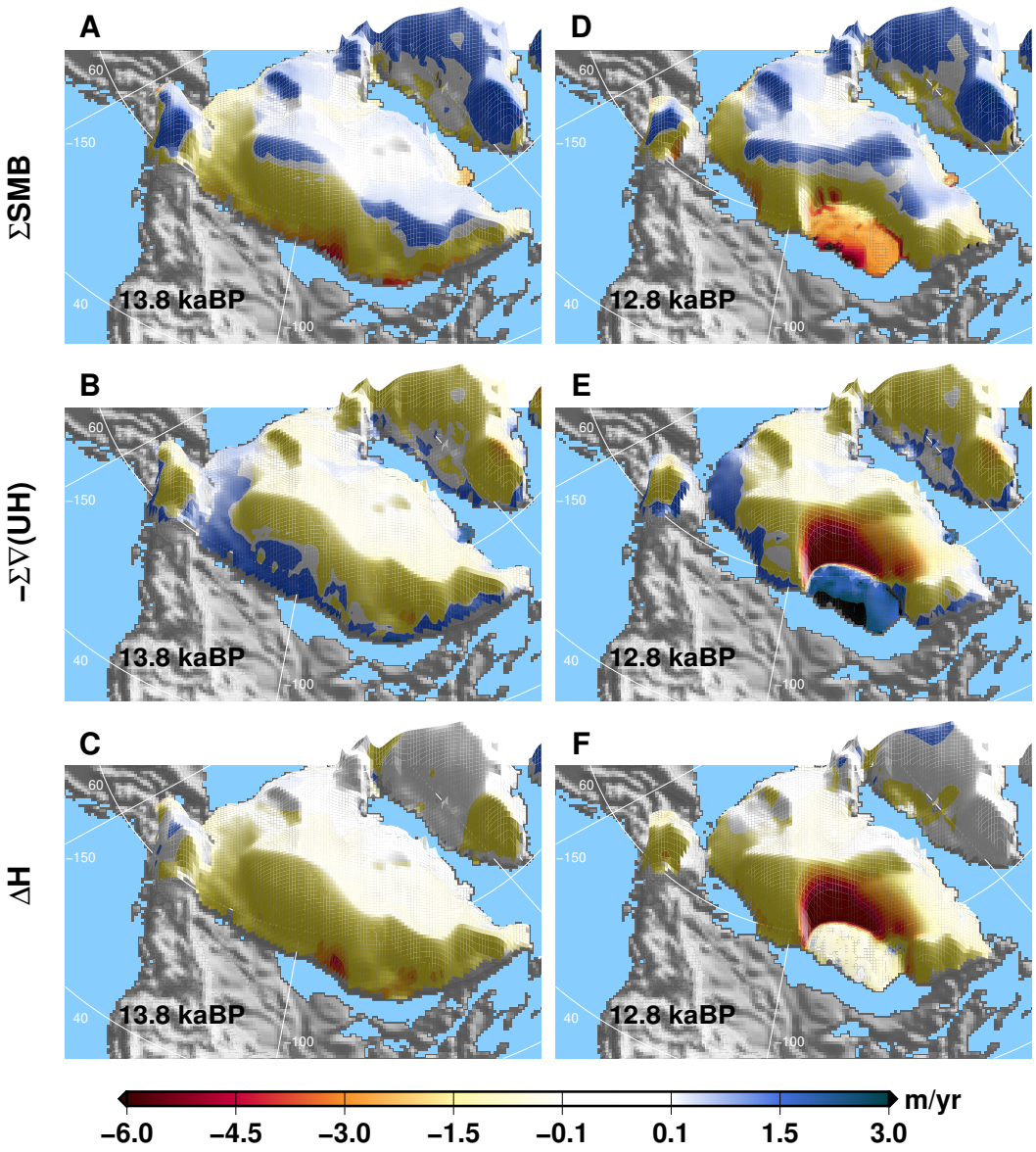

Figure S5. Respective role of surface mass balance with respect to ice dynamics. Total ice thickness change (expressed in metre per year) breakdown (Eq. 3) in the coupled experiment over a 100 year window: integrated surface mass balance (A,D), integral of the opposite of the ice flux divergence (B,E) and resulting change in ice thickness (C,F). The computations are done before (A,B,C, 13.8 kaBP – 13.7 kaBP) and after (D,E,F, 12.8 kaBP – 12.7 kaBP) the PLISI event.

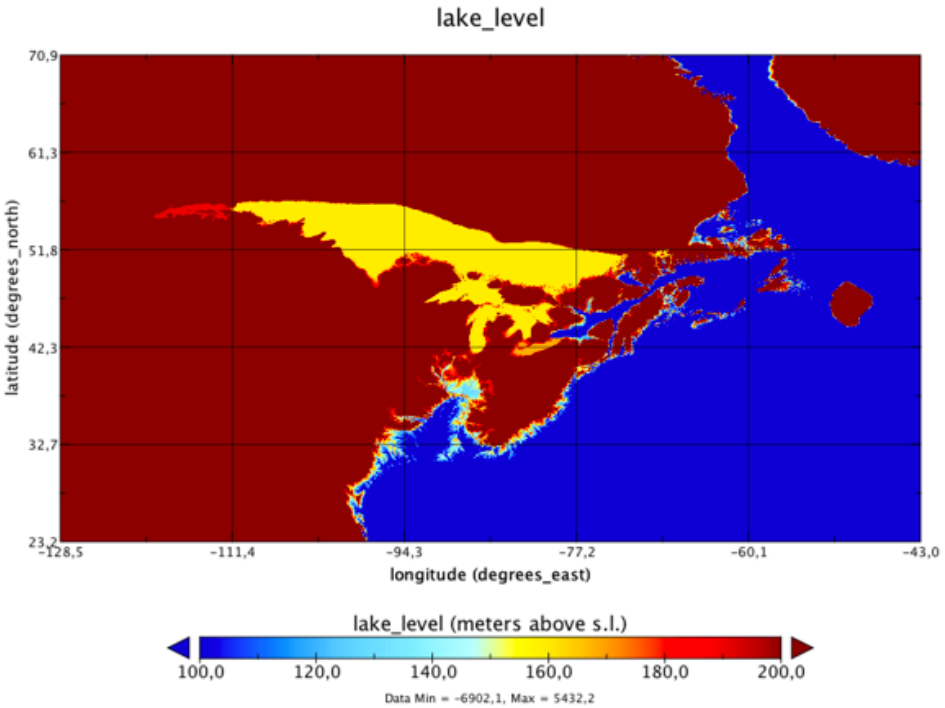

Figure S6. Example of a lake level computed using a 14 kaBP simulated ice sheet topography. The yellow area stands for a lake level at about 160 m above present-day sea level, so about 235 m above the 14 kaBP sea level.

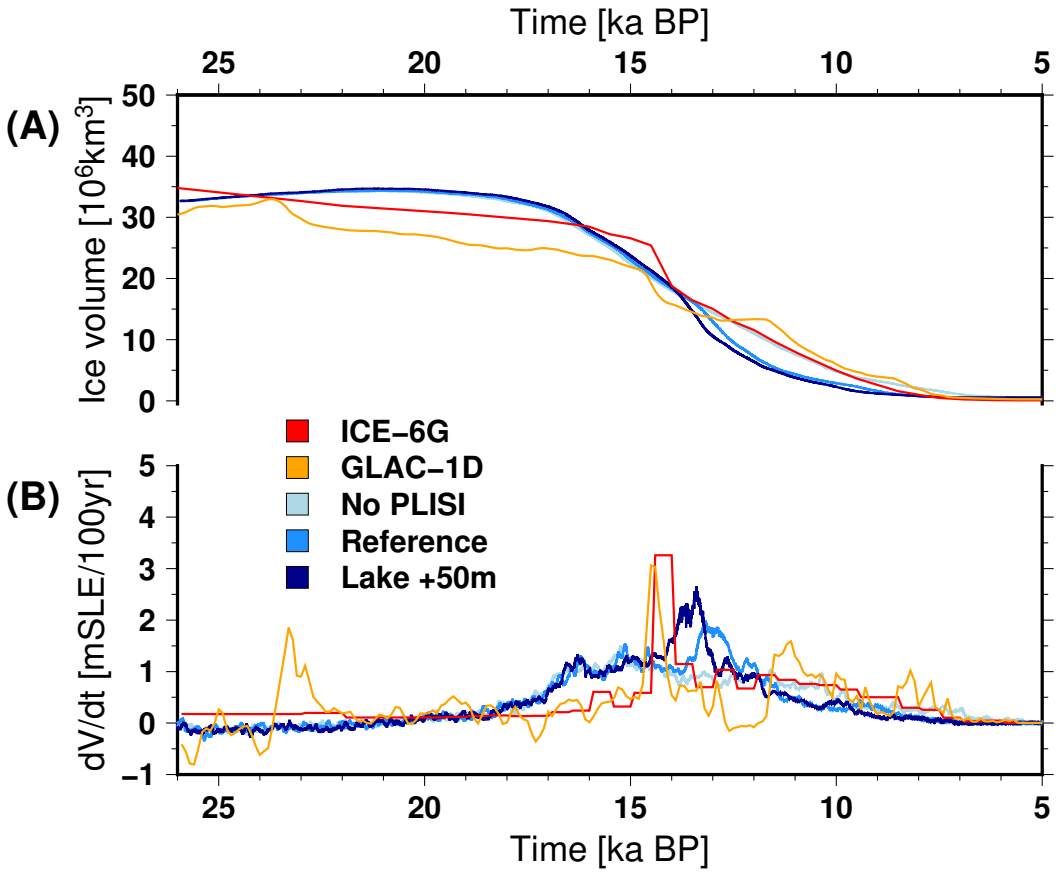

Figure S7. Importance of the PLISI for the temporal evolution. Simulated total ice volume (A) and rate of ice loss (expressed as ice volume contributing to sea level rise per century) (B) through the deglaciation (26 kaBP – 5 kaBP) for the NAIS using the GRISLI-iLOVECLIM set-up when we prevent the PLISI occurrence (light blue), in the standard configuration (lake level follows the eustatic sea level forcing, blue) and with a lake level at +50 metres above present-day at all times (dark blue). The ice sheet volume and rate of volume change of GLAC-1D and ICE-6G are shown in orange and red, respectively.

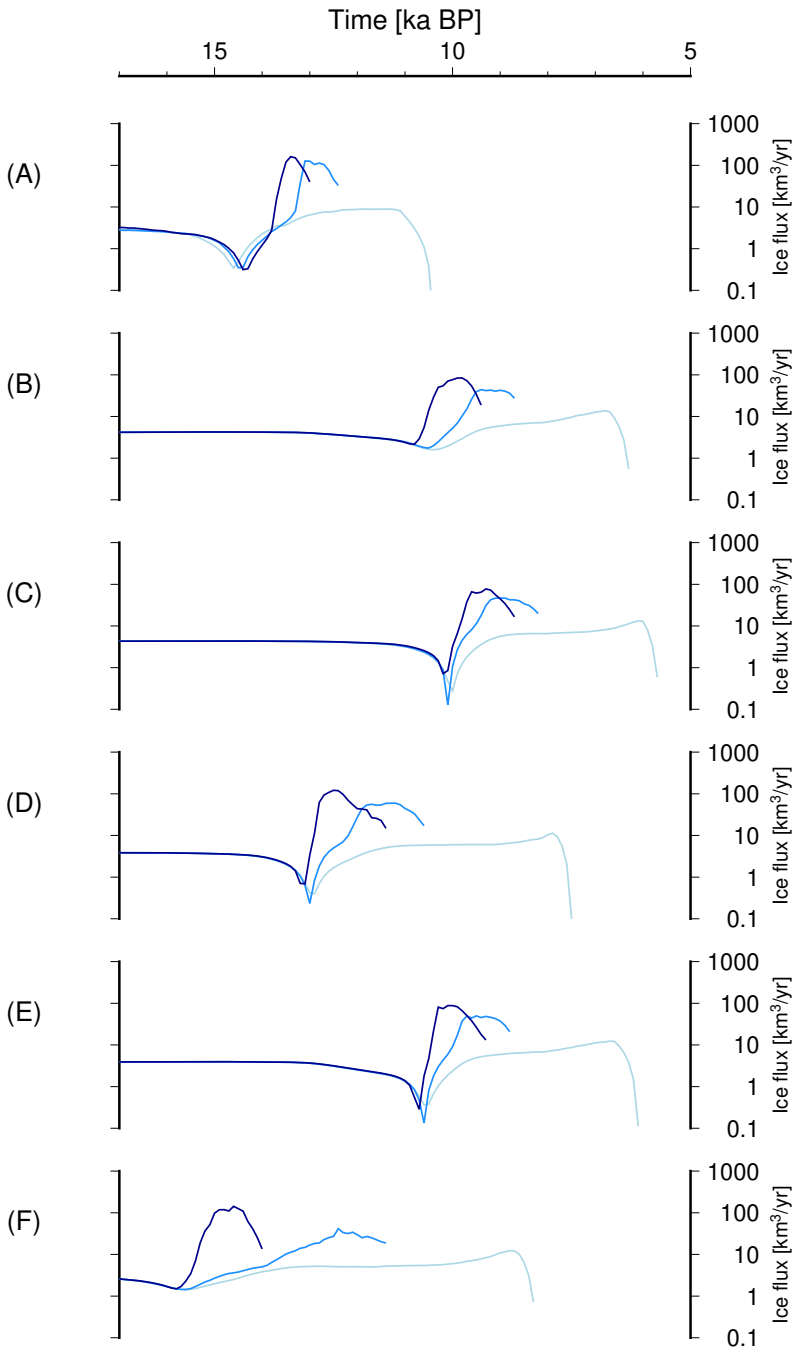

Figure S8. Importance of the PLISI for the ice flux. Simulated ice flux for a selected point affected by the PLISI (86.1 °W, 58.3 °N shown in Fig. S4) when we prevent the PLISI occurrence (light blue), in the standard configuration (lake level follows the eustatic sea level forcing, blue) and with a lake level at +50 metres above present-day at all times (dark blue) for the coupled experiment (A) and for a set of stand-alone ice sheet experiments forced by PMIP4 outputs: MPI-ESM-P (B), MIROC-ESM (C), FGOALS-g2 (D), IPSL-CM5A-LR (E) and GISS-E2-R (F). The stand-alone experiments here use a weighing factor for the fast variability of 0.25. The vertical scale is logarithmic. The curves stop when local ice thickness reaches zero.

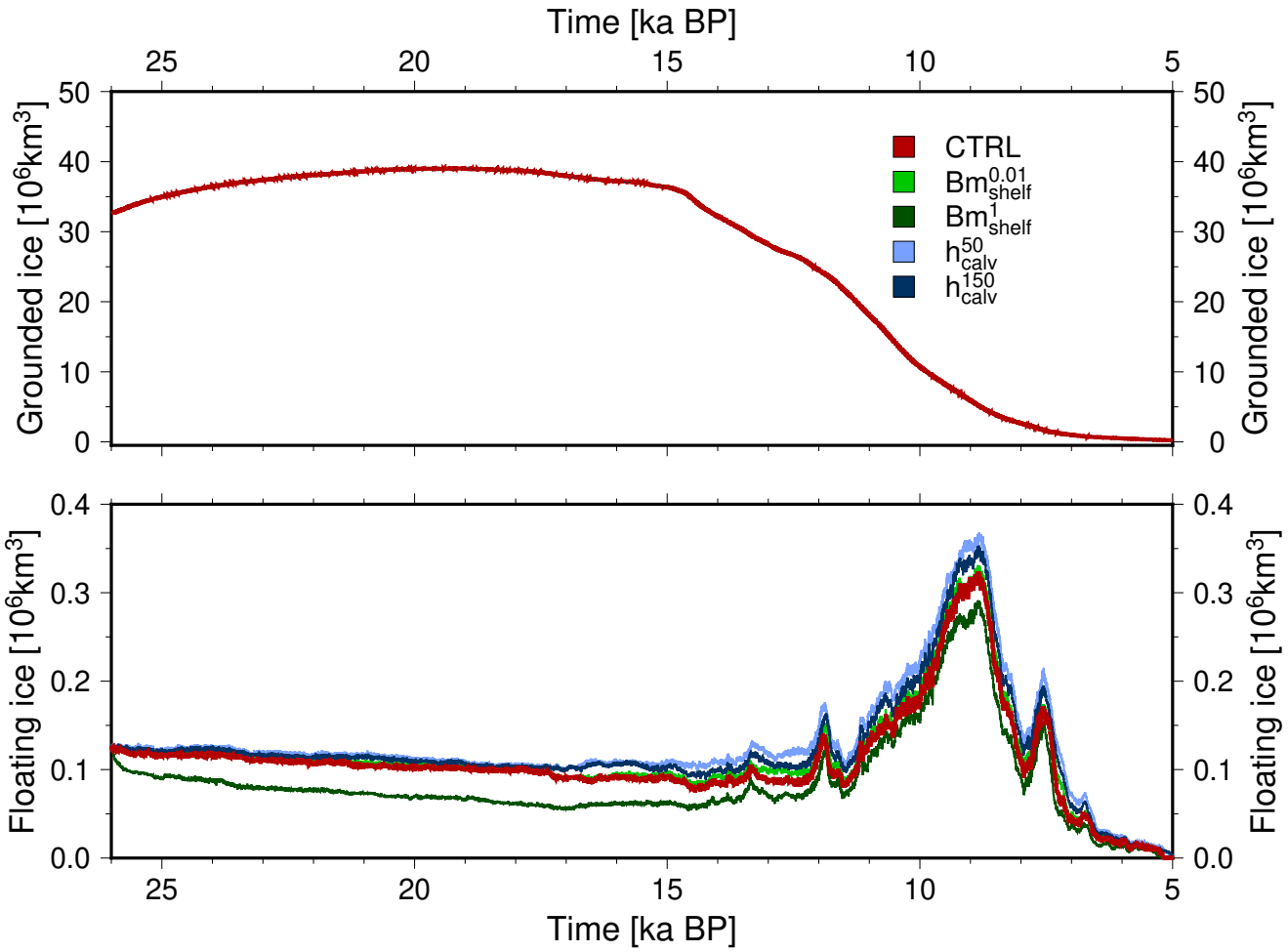

Figure S9. Importance of sub-shelf melt and calving rates. NAIS grounded ice volume (top) and volume of ice above flotation (bottom) for a set of sensitivity experiment. CTRL experiments for this figure is a stand-alone ice sheet simulation using the MPI-ESM-P climate anomalies with a weighing factor for the fast variabil ity of 0.25. The green curves represent experiments that use the same setup as the CTRL except that they have a constant sub-shelf melt rates of 0.01 m yr^{-1} (light green) and 1 m yr^{-1} (dark green) instead of using a time-varying sub-shelf melt rate (near 0 at the LGM and 0.3 for the pre-industrial). The blue curves also represent experiments that use the same setup as the CTRL except that they have an ice thickness threshold for calving of 50 m (light blue) and 150 m (dark blue) instead of 250 m in the CTRL.

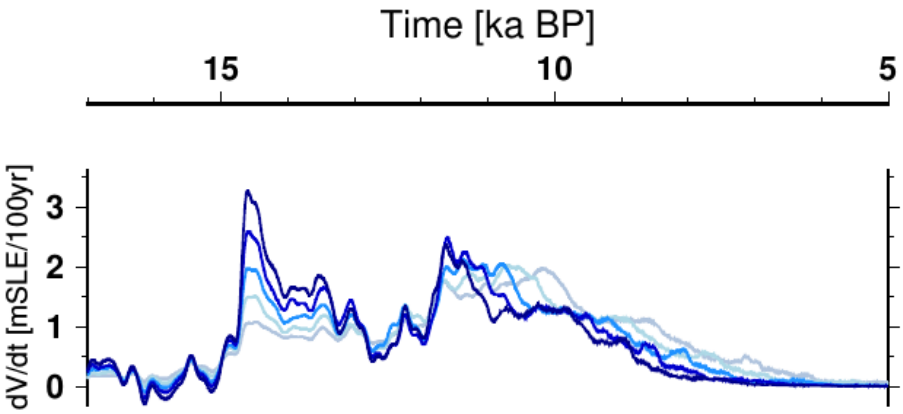

Figure S10. Importance of the fast variability weighing factor for stand-alone ice sheet simulations. Rate of NAIS ice loss through the deglaciation (17 kaBP – 5 kaBP) for stand-alone ice sheet simulations using MPI-ESM-P. The different curves are obtained with different value for the atmospheric fast variability weighing factor r (see Methods). The color gradients represent the importance given to the fast variability, from little importance (light grey, $r = 0.15$) to great importance (dark blue, $r = 0.55$).

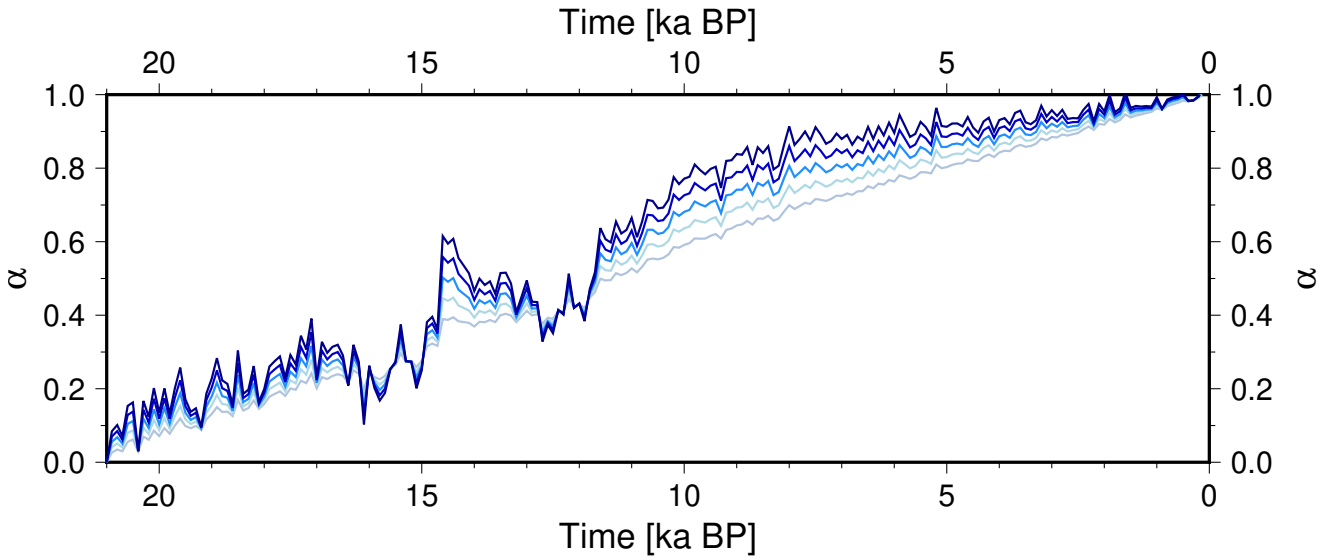

Figure S11. Glacial index used for the stand-alone experiments for a range of fast variability weighing factor r. The color gradients represent the importance given to the fast variability, from little importance (light grey, $r = 0.15$) to great importance (dark blue, $r = 0.55$).